THE JOURNAL OF PHYSICAL CHEMISTRY C
A JOURNAL OF THE AMERICAN CHEMICAL SOCIETY

pubs.acs.org/JPCC

Article

Model-Based Insight into Single-Molecule Plasmonic Mislocalization

Published as part of The Journal of Physical Chemistry virtual special issue "W. E. Moerner Festschrift".

Tiancheng Zuo, Harrison J. Goldwyn, David J. Masiello,* and Julie S. Biteen*

Cite This: *J. Phys. Chem. C* 2021, 125, 24531−24539

Read Online

ACCESS | Metrics & More | Article Recommendations | Supporting Information

ABSTRACT: Noble metal nanoparticles act as visible-wavelength antennas that reshape the emission of nearby dye molecules. Because single-molecule imaging overcomes ensemble averaging, it is uniquely suited for understanding these plasmonic effects. We have engineered single-particle assemblies consisting of a gold nanodisk surrounded by ATTO590 dye molecules attached by double-stranded DNA linkers. These assemblies provide a controlled geometry that places plasmon-coupled dye molecules at specific radial positions in the plane of the nanodisk and provides the ground truth actual dye molecule position for further analysis. We modeled the molecule−nanoantenna interaction as two coupled dipoles and propagated their interfering fields through a diffraction-limited microscope to generate a coupled-dipole image that accurately recreates the distorted PSFs seen in numerical simulations of plasmon-enhanced single-molecule fluorescence. We fit simulated and experimental data to the model function as well as to a standard Gaussian function and evaluated the advantages of the model approach. Overall, we find that the image model can better recapture certain aspects of the dye molecule mislocalization, and we propose that remaining gaps can be addressed by integrating higher-order plasmon multipole effects into the nanodisk response as well as by simultaneously using both image and spectral information.

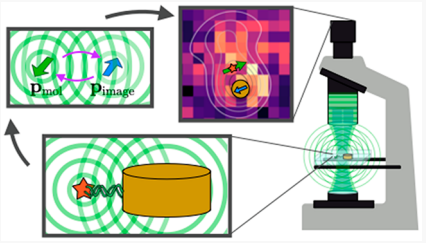

INTRODUCTION

Noble metal nanoparticles support localized surface plasmon resonances that interact strongly with free-space light and enhance the electromagnetic field in their vicinity. This concentration of radiation has been exploited for applications in sensing, spectroscopy, and catalysis, among many others, and has been used to engineer the emissive properties of nearby dye molecules.[1−4] One promising application is the use of plasmonic nanoparticles to enhance the resolution for bioimaging[5] and hot-spot mapping.[6−8] Single-molecule fluorescence microscopy enables the detection of individual dye molecules, and single-molecule spectroscopies have further characterized their fluorescent properties.[9−11] Because single-molecule imaging overcomes ensemble averaging to reveal properties of each dye, it is uniquely suited for understanding how interactions with plasmonic nanoparticles reshape the emission of nearby dye molecules.[12]

Typically, the raw images obtained from single-molecule microscopy are superlocalized based on finding the center of the diffraction-limited emission pattern (point-spread function, PSF) detected on a camera.[13,14] The localization precision of this center position can be improved by fitting the pattern to a Gaussian distribution or an Airy function using a weighted least-squares fit or maximum likelihood estimation[15] as well as by increasing the number of detected photons and the measured signal-to-noise ratio.[13] However, the assumption that the most intense point of the emission pattern in the image plane corresponds to the most likely location of the emitter in the focal plane (i.e., the most likely molecule position) relies on the assumption that near-field coupling and far-field interference between the emitter and its surrounding environment are minimal. Thus, because the local and radiative electromagnetic properties are strongly influenced by a plasmonic nanoparticle, the emission PSF will be distorted for dye molecules located in the near field of these antennas.[6,7,9,16−24] Consequently, the center of the distorted PSF may not indicate the true location of the single emitter. This mismatch between the true emission center and the image centroid is also called *mislocalization*.[25]

Another way to explain the modification of the emission pattern is that the plasmonic nanoantenna alters the local density of states of proximal single emitters.[7] The extent of mislocalization in a nanoparticle−molecule coupling geometry can be as large as 30−50 nm either toward (inward) or away from (outward) the plasmonic particle.[7,17,20,21] Evidence suggests that this mislocalization is a result of emission coupling[7,16,21] and that the plasmon enhancement of absorption affects only the population of the excited state and thus the overall image intensity. Using a dye with an

Received: September 9, 2021
Revised: October 18, 2021
Published: November 2, 2021

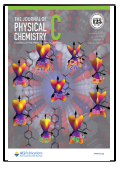

https://doi.org/10.1021/acs.jpcc.1c07989
J. Phys. Chem. C 2021, 125, 24531−24539

emission spectrum largely blue-shifted relative to the localized surface plasmon resonance (LSPR) of the plasmonic particle can avoid mislocalization to a great extent and still achieve enhancement through absorption coupling.[18,26] However, the line width of both the LSPR and the single-molecule emission spectrum are broad, which makes it harder to separate the emission coupling from absorption. Additionally, enhancement is largely weakened without the emission coupling.[2,3,27]

Over the past decade, theoretical ideas have been proposed to explain the mislocalization phenomenon, but no model has been fit to data in attempt to infer the known molecule position in the presence of a nearby plasmonic antenna. Most approaches have assumed that the distorted PSF must result from interference between the emitting molecule and the image-dipole created in the responding nanoantenna.[7,17,20] However, in the case of super-resolution surface-enhanced Raman scattering, generalized Mie theory has demonstrated that mislocalization can also result from interference of higher-order multipoles excited in the plasmonic structure.[19] Here, it is understood that fluorescence is usually quenched,[4,28−30] as surface-enhanced Raman scattering contributes the dominant signal for close molecule−nanoantenna separations (generally <10 nm).[19,31] Other researchers have tested nonmechanistic models of the multilobed PSF that occurs when a dye molecule couples to plasmonic antenna,[23,27] but recently, mechanistic models have shown promise as a descriptive tool:[9,17] by modeling the molecule−nanoantenna interaction as two coupled dipoles and propagating their interfering fields through a diffraction-limited microscope, a coupled-dipole image can be generated that accurately recreates the distorted PSFs seen in numerical simulations of plasmon-enhanced single-molecule fluorescence.[9,17]

However, one challenge in validating the use of this model to extract the true molecule position from experiment is the difficulty of designing a single-molecule experiment that encodes the ground truth position of the molecule.[21,32−34] One promising approach to this challenge has been to position fluorescent molecules near plasmonic nanoparticles with DNA origami,[21,33] and this approach was extended to increase throughput based on spherical dye−nanoparticle assemblies.[35] Here, we present a new geometry for studying plasmonic mislocalization effects based on leveraging electron beam lithography and DNA nanotechnology to create a carefully controlled geometry that places dye molecules at a fixed and known radial distance from a gold nanodisk and positions the dye molecules in the imaging plane. This geometry enables a high throughput single-molecule experiment that provides abundant data for analysis. We interpret the mislocalization effect in this coupled system by applying a coupled-dipole interference model[17] to the measured data and use it to extract the molecule location and orientation. On the basis of plasmon-enhanced super-resolution images generated by simulation and computed at high magnification, we find that the model reliably retrieves the location and orientation of the dye molecule with an error significantly less than the standard Gaussian fitting for dye−nanodisk separations of ∼50 nm and beyond. However, at the shorter ∼10 nm dye−nanodisk separation distances and the image resolution used experimentally, the model struggles to locate the dye for both simulation-generated and experimental data due to the increasing importance of higher-order plasmonic effects absent in the coupled dipole model. Nevertheless, this work provides a first step in the direction of model-based single-molecule super-resolution imaging that will be expanded upon in future work to simultaneously incorporate both emission spectra and microscope images together with higher-order multipole effects in the model.

MATERIALS AND METHODS

Gold Nanodisk Fabrication. Poly(methyl methacrylacte) (PMMA, Michrochem, 200 nm) was spin-coated on a glass coverslip, and then an 8 nm gold thin film was thermally deposited on top of the PMMA to make a conductive layer for electron-beam writing (Angstrom Engineering, Evovac evaporator). Electron beam lithography (110 kV, 1000 pA; JEOL JBX 6300FS) was used to pattern circles in the layers. The conductive gold layer was removed with gold etch (KI and iodine), and then the resist was developed in 1:3 methyl isobutyl ketone:isopropanol (IPA). The sample was cleaned with IPA. Onto the sample were deposited 2 nm Cr, 30 nm Au, 2 nm Cr, and then 20 nm SiO_2 by electron-beam evaporation (Denton Enerjet evaporator). Finally, the sample was soaked in 60 °C acetone overnight for the lift-off. The remaining PMMA was lifted off, leaving arrays of 30 nm high cylindrical gold nanodisks with an SiO_2 cap and Cr wetting layers (Figure 1a).

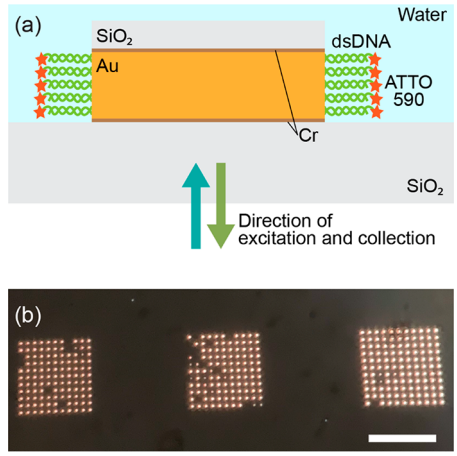

Figure 1. (a) Sample geometry schematic (not to scale) and (b) dark-field image of nanoparticle arrays (left to right: 70, 76, and 86 nm nanoparticles; 11 × 11 array of particles with 2 μm center-to-center spacing. Scale bar: 15 μm. Only bright particles were used for further characterization.

Three 11 × 11 arrays of nanodisks with 2 μm center-to-center spacing were designed with nominal particle diameters of 70, 80, and 90 nm, respectively (Figure 1b). The size and shape of gold nanodisks were confirmed after all experiments were completed by a scanning electron microscope (SEM) with 5 kV accelerating voltage and 6600 nA (SU8000, Hitachi High Technologies America, Inc.).

Spectroscopic Ellipsometry. The SiO_2 cap thickness and refractive index were characterized by variable angle spectroscopic ellipsometry (Woollam M-2000 ellipsometer) of a reference substrate: a large bare coverslip was coated by electron-beam evaporation (Denton Enerjet evaporator) with gold and SiO_2 under the same conditions as for the nanodisk fabrication.

Dark-Field Scattering Spectroscopy. The nanodisks were designed with nominal particle diameters of 70, 80, and 90 nm. To determine the exact size, we compared the dark-field scattering spectra of the nanodisks to full-field electro-

https://doi.org/10.1021/acs.jpcc.1c07989
J. Phys. Chem. C 2021, 125, 24531−24539

magnetic simulations of the nanodisk scattering. For scattering spectroscopy, the arrays were immersed in water, and dark-field scattering spectra were collected for individual nanodisks (Supporting Information Figure S1) by using an inverted microscope (Olympus IX71) in dark-field configuration and a monochromator. Each array was excited with a broadband halogen lamp through a water-immersion dark-field condenser, and scattered light was collected through a dark-field oil-immersion objective (NA = 0.6). The nanodisk image was aligned to the entrance slit of an imaging spectrograph (Acton 2300, Princeton Instruments), and spectral data were collected on an electron multiplying charge-coupled device (EMCCD) (1 s integration time, electron-multiplying gain 100; Andor iXon). Background spectra collected from nearby positions with no nanodisk on the spectrograph entrance slit were subtracted from measured spectra, and all data were divided by the broadband spectrum of the halogen light source and any additional neutral density filters to correct for the system spectral efficiency.

Simulations of Nanodisk Scattering Spectra. Nanodisk spectra were simulated by finite-difference time-domain simulation of the full sample geometry (Ansys Lumerical FDTD Solutions software package). All simulations were performed with the nanodisk immersed in water and placed on a glass slab. The total simulation volume was 3.375 μm^3; near the nanodisk, a fine-mesh grid with 3.375 nm^3 cell volume was used. Water and glass were modeled with a constant refractive index of $n = 1.333$, $k = 0$ and $n = 1.5$, $k = 0$, respectively. The frequency-dependent complex permittivity of Au and Cr was obtained by an analytical fit to experimental data.[36] The SiO_2 permittivity was attained by spectral ellipsometry. The nanodisk diameters were determined by varying the simulated cylinder radius and matching the simulated far-field scattering spectra to the experimentally measured dark-field scattering spectra (Figure S1).

Dye Conjugation. ATTO590 dye−Au nanodisk assemblies were created with double-stranded DNA (dsDNA) linkers.[35,37,38] 5 μL of 100 μM thiolated single-stranded DNA was mixed with an equal amount of complementary ATTO590 single-stranded DNA (Table S1). Ethylenediaminetetraacetic acid-tromethamine (Tris-EDTA, 80 μL, pH 8) was added. The solution was hybridized at 95 °C for 2 min followed by incubation at room temperature for 1 h. 10 μL of 1 M dithiothreitol (DTT; 15 mg in 100 μL of Tris-EDTA buffer) and 130 μL of Tris-EDTA buffer were added to the solution for an hour to reduce the disulfide group. An NAP-5 column (GE Healthcare Life Sciences) was then used to separate the DTT from the thiolated dsDNA. 1 mL of the DNA solution was immediately added to a beaker that with the nanodisks coverslip. 9 mL of Tris-EDTA was added, and the sample was incubated for 1 h. 100 μL of 0.1 M phosphate buffer (1/10 by volume) and 1 μL 10% sodium dodecyl sulfate (1/1000 by volume) were added to reduce the nonspecific binding of dyes to the coverslip. The sodium chloride concentration in the solution was gradually brought up to 0.5 M over 3 h to increase the DNA loading. Finally, the coverslip was sonicated in deionized water three times to eliminate unbound dsDNA and dried with high-pressure nitrogen gas.

Single-Molecule Imaging by dSTORM Microscopy. Direct stochastic optical reconstruction microscopy (dSTORM)[39] was performed as previously published.[35] Briefly, a 561 nm CW laser was used as the excitation light source (Coherent CUBE). The nanodisk−DNA assemblies were immersed in 100 μL of dSTORM imaging buffer (100 μL of 500 mM 2-mercaptoethanol at pH 9). The sample was illuminated with high laser power (40 $\mu W/\mu m^2$) to make dyes enter a dark state and then was imaged at lower power densities (12 $\mu W/\mu m^2$).[40] Images were recorded on a 512 × 512 pixel Andor iXon EMCCD camera (1000 electron-multiplying gain; 100 ms integration time). Imaging was done with a 100× 1.3 NA oil-immersion objective and a 3.3× beam expander; in this geometry, one camera pixel corresponds to 48.5 nm.

Simulations of Plasmon-Coupled Dye Emission. Frequency-domain electromagnetic simulations using the MNPBEM17 Toolbox[41] were performed to parametrize the analytical model. Each nanodisk was modeled as an oblate spheroid of height h = 36.82 nm and diameter d = 91.00, 98.53, and 110.53 nm to best fit the experimental spectra of the 70, 76, and 86 nm nanodisks, respectively (Supporting Information). Tabulated gold dielectric data from Johnson and Christy[36] were used for all calculations along with a constant background refractive index of $n = 1.333$ and $k = 0$ for water. The numerically fit images were generated by taking the MNPBEM-calculated far fields on a hemisphere of radius 0.2 cm and numerically calculating the focused and diffracted image fields by using the Debye−Wolf formalism.[9]

RESULTS AND DISCUSSION

Substrate Characterization. Plasmon-coupled fluorescence depends strongly on the dye−nanoparticle separation distance. Experimental and computational studies of gold nanoparticles have shown that ∼10 nm separation distances are optimal for reducing fluorescence quenching while achieving high plasmon enhancements.[29,30,35] Gold nanodisks were made by electron beam lithography on top of glass microscope coverslips, and a layer of SiO_2 was evaporated on top of the nanodisks, leaving gold exposed only on the nanodisk sides (methods). The SiO_2 cap was characterized by spectroscopic ellipsometry of a reference substrate. The layer thickness and refractive index were extracted from a fit of the measurement to a two-layer model (Figure S2). We created ATTO590 dye−nanoparticle assemblies in which the dye molecules were positioned in the nanodisk plane, and the radial separation distance was maintained at 10.2 nm by using double-stranded DNA (dsDNA) spacers and a thiol linkage (methods, Figure 1a). Because the persistence length of dsDNA is >40 nm in buffered solutions,[42] this 10.2 nm spacing was achieved with dsDNA spacers of 30 base pairs (Table S1).

The nanodisks were designed with nominal diameters of 70, 80, and 90 nm. The actual sizes were determined by comparing the single-particle spectra (blue curves in Figure 2a−c and Figure S1) to FDTD simulated spectra for nanodisks of the same materials and thickness but varying diameter (methods). The experimental scattering peaks best match FDTD peaks for diameters of 70, 76, and 86 nm (pink lines in Figure 2a−c). The nanodisk sizes and shapes were confirmed by SEM after all experiments were completed (Figure 2a−c insets).

Super-Resolution Imaging of Mislocalized Emission from Dye Molecules around a Single Plasmonic Nanodisk. Plasmon-coupled fluorescence is also a resonant process that is maximized when the fluorescence absorbance and emission wavelengths overlap with the wavelength of the nanoparticle LSPR. The gold nanodisk sizes were chosen to sustain plasmon resonances that overlap with the ATTO590

https://doi.org/10.1021/acs.jpcc.1c07989
J. Phys. Chem. C 2021, 125, 24531−24539

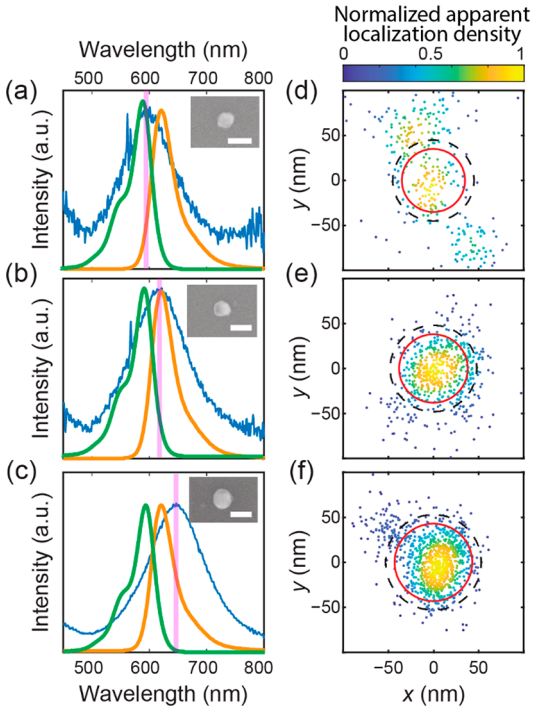

Figure 2. Single-particle experimental mapping. (a−c) Spectra of representative single 70, 76, and 86 nm gold nanodisks, respectively. The experimental dark-field spectra (blue curves) and peak scattering wavelength from FDTD simulations (pink lines) are shown for each nanodisk size. Green and orange curves: ATTO590 absorption and emission spectra, respectively (data from IDEX Health & Science, LLC). Insets: SEM images of representative single gold nanodisks; scale bars: 100 nm. (d−f) Localizations of dye molecules placed 10.2 nm from the edge of the gold nanodisk in panel a, b, or c, respectively. Each point represents the apparent position of one dye molecule based on a 2D Gaussian fit to a background-subtracted single-molecule fluorescence image. Red circles: actual diameter of the nanodisks; black dashed lines: actual radial position of the dye molecules in that assembly.

spectrum (Figure 2a−c). We hypothesized that the most plasmon coupling, and therefore the strongest mislocalization, would be observed for the 76 nm nanodisks, which have the best spectral overlap, and we also predicted that the dye molecules would still couple to the 86 nm nanodisks due to their larger size and thus their stronger local surface plasmon mode.[5]

Under constant 561 nm laser excitation, ATTO590 molecules stochastically turn on and off in the dSTORM redox imaging buffer, which enables single-molecule detection.[40] We measured the mislocalization distortion in each system by comparing the known radial positions of the ATTO590 molecules (black dashed lines in Figure 2a−c) to the apparent positions measured one at a time in our epifluorescence single-molecule microscope via dSTORM (points in Figure 2d−f).[35,40] The off-frames (background from constant low-intensity fluorescence from the nanodisk only) were distinguished from the on-frames (single ATTO590 molecule bursts) in the raw data. Frames in which no single molecule bursts were detected served as background images, and the nanodisk center position was found by fitting the average of 50 background images to a 2D Gaussian function; we corrected for system drift by determining this position every 50 frames. The average background image from the nearby off-frames was subtracted from each on-frame with the SMALL-LABS algorithm.[14] Each background-subtracted single-molecule image was fit to a 2D Gaussian function to find the apparent localization position. Figure 2d−f shows the localization density maps for all the localizations about one representative nanodisk for each of the three different sizes. Each point indicates the apparent position of one dye molecule in a 100 ms imaging frame, and the normalized localization density for each point is given by the number of neighboring points within a 25 nm radius circle normalized by the area of that circle.

Despite the localization error (±10−20 nm in these experiments), if there were no mislocalization, the most likely position for molecular detections would be along the black dashed circle 10.2 nm from the nanodisk edge. However, the apparent position distributions in Figure 2d−f show that the most likely (yellow) apparent position is in fact substantially mislocalized toward the nanodisk center. These single-particle super-resolution images were, however, insufficiently sampled for further analysis.

Quantification of Mislocalized Emission Based on Compiled Nanodisk−Dye Assemblies. To overcome the inhomogeneity that arises from undersampling in Figure 2d−f, we measured the localizations from the dye molecules in each of 12 nanodisk−ATTO590 assemblies. These 2000−8000 single-molecule fluorescence localizations for each nanodisk diameter were combined based on the nanodisk center positions. These compiled localization maps (Figure 3a−c) show the same mislocalization that was qualitatively revealed in Figure 2: in Figure 3a−c, most of the molecules are mislocalized toward the nanodisk center. Because Figure 3a−c shows some asymmetry due to undersampling, the corresponding radial localization densities are plotted in Figure 3d−f: the radial localization density is defined as the number of localizations within each 10 nm radial distance interval normalized by the area of the corresponding radial ring. The dashed vertical lines show the actual radial location of the dye molecules. For all three nanodisk sizes, over 75% of the localizations appear shifted inward from the black circles and >5% are mislocalized outward from the black circles. Indeed, this mislocalization increases with nanodisk size: as the nanodisk size gets larger, a higher percentage of the apparent localization positions fall to the left of the dashed vertical lines, i.e., toward the nanodisk center, and for the 86 nm nanodisk assemblies, the most probable position is shifted by 50 nm: all the way to the nanodisk center (Figure 3f). The fact that the mislocalization increases with increased nanodisk size despite the decrease in spectral overlap (Figure 2a−c) indicates that the high plasmon resonance strength of the larger nanodisks plays an important role in the mislocalization effect and also indicates that the spectral overlap between the ATTO590 emission spectrum and the local surface plasmon mode is more important than the overlap in absorption spectra (Figure 2c).

In addition to quantifying the radial mislocalization, we measured the single-molecule fluorescence intensity enhancement at each apparent radial position by normalizing the average intensity of the molecules apparently located within each 20 nm radial interval by the average intensity of ∼10% of the molecules in Figure 3d−f appearing at the actual molecule position (which are not mislocalized and therefore not coupled to the nanodisk). Overall, we find a general trend in Figure S3 that the molecules that appear mislocalized farthest inward have the highest fluorescence intensities. Furthermore, despite

https://doi.org/10.1021/acs.jpcc.1c07989
J. Phys. Chem. C 2021, 125, 24531−24539

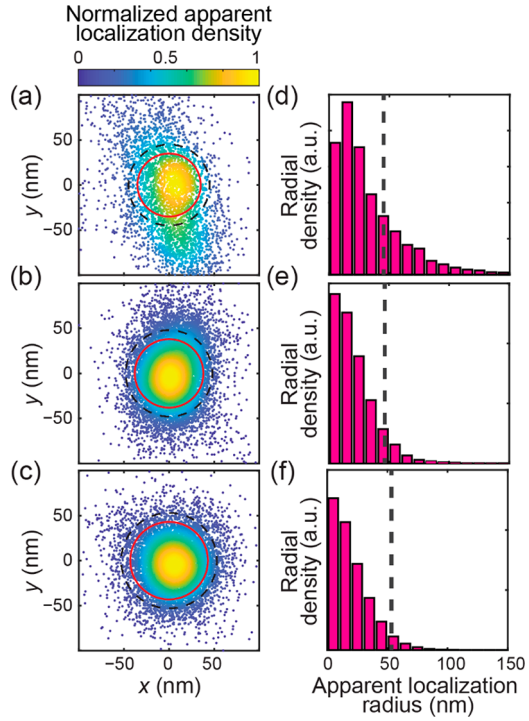

Figure 3. Compiled experimental heat maps. (a–c) Localizations of dye molecules placed 10.2 nm from the edge of gold nanodisks with 70, 76, and 86 nm diameters, respectively. Each point represents the apparent position of one dye molecule based on a 2D Gaussian fit to a background-subtracted single-molecule fluorescence image. The colorbar indicates the normalized apparent localization density. Each plot compiles the localizations from 2000–8000 single-molecule fluorescence images from molecules around 12 nanodisks. (d–f) Radial localization density histograms corresponding to the scatter plots in panels a–c. The black dashed lines indicate the actual radial position of the dye molecules in that assembly.

the large mislocalizations (Figure 3), we find only very subtle fluorescence enhancements in Figure S3. In particular, though the 86 nm nanodisks show the greatest mislocalization (Figure 3f), the dye fluorescence is mainly quenched (Figure S3). This result for the nanodisks that are red-shifted from the ATTO590 absorption spectrum (Figure 2c) is consistent with past studies that have shown that the emission intensity enhancement is affected by the overlap of the nanoparticle LSPR with both the absorption and emission spectra of the dye molecules, whereas the mislocalization results mainly from emission coupling.[16]

Coupled-Dipole Modeling of Emission. The measured single-molecule images were further interpreted by modeling the effects of a plasmonic nanoantenna on each proximal dye molecule as a pair of near-field coupled dipoles that radiate to the far-field.[9,17] The microscopy experiment measures the superposition of the two emission processes (direct emission by the molecule and scattering from the nanodisk) as well as a cross term that accounts for interference between these two sources. This cross term, which depends on the relative orientations of the molecule and plasmonic nanodisk, heavily influences the mislocalization.[17]

We modeled the molecular emissive transition dipole $\mathbf{p}_0$ and the induced plasmon dipole $\mathbf{p}_1$ by the following coupled dynamical equations:

$$\mathbf{p}_0 = \boldsymbol{\alpha}_0 \cdot (\mathbf{E}_F + \mathbf{E}_1(\mathbf{x}_0)) \quad (1)$$

$$\mathbf{p}_1 = \boldsymbol{\alpha}_1 \cdot \mathbf{E}_0(\mathbf{x}_1) \quad (2)$$

where the molecule and nanodisk linear dyadic polarizabilities are $\boldsymbol{\alpha}_i$ (i = 1, 2). The fictitious harmonic field $\mathbf{E}_F = E_0 \hat{\mathbf{e}}_x e^{-i\omega t}$ drives only $\mathbf{p}_0$, which forces both dipoles to oscillate harmonically and represents the continuous population of the molecule's emissive state by absorption of the excitation laser and subsequent fluorescence relaxation. The molecule and plasmon mode are coupled by the fully retarded dipole fields, $\mathbf{E}_i(\mathbf{x}_j) = \mathbf{G}(\mathbf{x}_j, \mathbf{x}_i) \cdot \mathbf{p}_i$, generated by the ith dipole evaluated at the location of the jth dipole; here $\mathbf{G}$ is the standard electric dipole relay tensor.[39] Upon substituting $\mathbf{E}_i(\mathbf{x}_j)$ for the dipole fields in eqs 1 and 2, the coupled equations are solved to yield the complex dipole moments containing both oscillation magnitude and phase as functions of the polarizabilities and dipole–dipole orientation.[9]

Solution of the coupled dipole equations (eqs 1 and 2) requires definition of the dyadic polarizabilities $\boldsymbol{\alpha}_0$ and $\boldsymbol{\alpha}_1$. This information can be attained by parametrization against the spectra of the uncoupled molecule and nanodisk.[9,17] Specifically, we model the molecule's emissive dipole transition by a Lorentz oscillator polarizable only in the direction of the arbitrary molecular orientation, i.e., $\boldsymbol{\alpha}_0 = \hat{\mathbf{e}}_x \alpha_{mol} \hat{\mathbf{e}}_x$ in the reference frame of the molecule. We approximate the nanodisk by an oblate spheroid in the modified long-wavelength approximation,[43] with polarizability $\boldsymbol{\alpha}_1 = \hat{\mathbf{e}}_x' \alpha_{long} \hat{\mathbf{e}}_x' + \hat{\mathbf{e}}_y' \alpha_{long} \hat{\mathbf{e}}_y' + \hat{\mathbf{e}}_z' \alpha_{short} \hat{\mathbf{e}}_z'$ in the basis aligned with the nanodisk

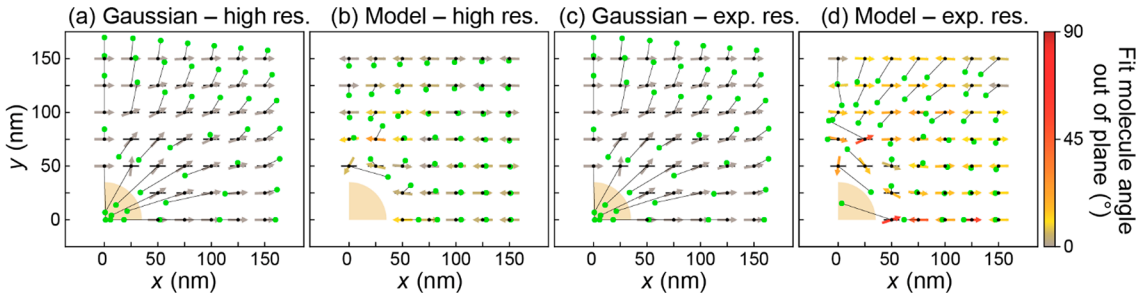

Figure 4. Fit positions for simulated dipole oscillators in the plane of a 76 nm gold nanodisk modeled as an oblate spheroid. The black dots indicate the ground truth positions of molecular oscillators oriented in-plane along the x-axis (black horizontal lines). The green dots indicate the apparent emission position of each molecule after a fit to (a, c) a Gaussian distribution or (b, d) the coupled-dipole image model, and the arrows indicate the predicted molecule orientation projected into the plane of the nanodisk with the color measuring its predicted out-of-plane projection. The colorscale is chosen to highlight the small number of significantly out-of-plane localizations. The images to fit were simulated at (a, b) a high resolution of 3.3 nm/pixel as well as at (c, d) the experimental resolution of 48.5 nm/pixel.

https://doi.org/10.1021/acs.jpcc.1c07989
J. Phys. Chem. C 2021, 125, 24531–24539

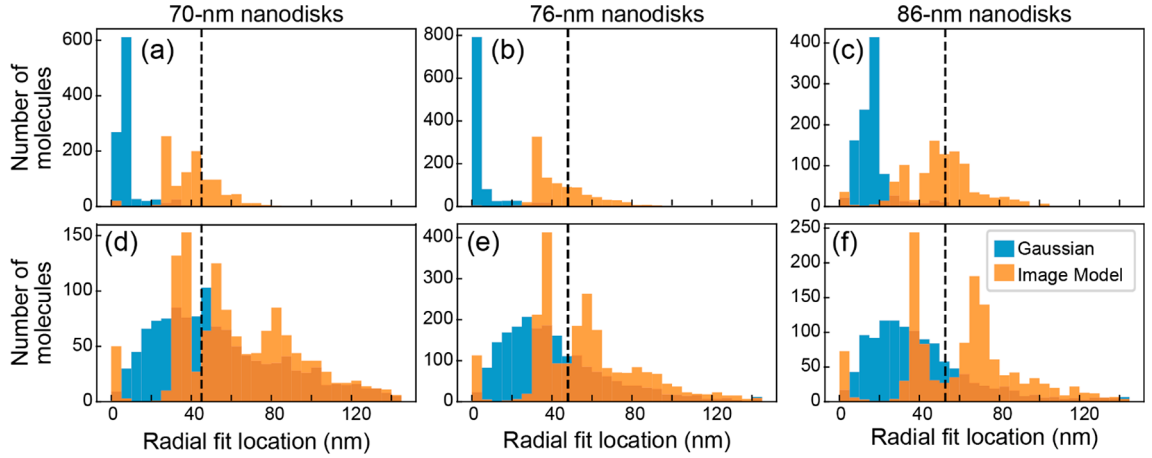

Figure 5. (a–c) Simulated and (d–f) experimental images of single ATTO590 dye molecules coupled to 70, 76, and 86 nm oblate spheroids, respectively, are fit to a standard 2D Gaussian function (blue) and the coupled-dipole image model (orange) to derive the apparent radial localization density histograms for each fitting function. The black dashed lines indicate the actual radial position of the dye molecules in each assembly.

principal axis. While the latter is an idealization of the true nanodisk geometry, it enables a closed form solution of Maxwell's equations, including the effects of radiation damping for the nanodisk long- and short-axis dipolar LSPRs. The plasmonic excitations along these axes depend upon the Drude parameters describing the electronic responses of bulk gold as well as upon the two semiradii of the nanodisk.

With the dipole polarizabilities defined, the fields radiated by the model molecule and nanodisk follow. But to model the microscopy images, the dipole fields must be focused and diffracted through an idealized microscope. To this end, we analytically evaluated the Debye–Wolf integral of the far fields scattered by the near-field coupled dipoles in eqs 1 and 2. The resulting image contains the superposition and interference of the focused and diffraction-limited fields, $\mathbf{E}_0^{\mathrm{im}}$ and $\mathbf{E}_1^{\mathrm{im}}$, which are proportional to each dipole moment, respectively. This analytical image model can therefore be incorporated as a fit function to reduce the mislocalization caused by fitting to the more simplistic Gaussian function. For the numerical simulations used to test the analytical image model, the radiated fields are transformed to image fields by numerically evaluating the Debye–Wolf integral.

Retrieving the Location and Orientation of the Dye Molecules with Model and Gaussian Fits. As a first test of the model, we simulated a collection of dye molecules ($\mathbf{p}_0$) near gold oblate spheroids ($\mathbf{p}_1$) that were fit to experimental data of the uncoupled dye emission and plasmon scattering spectra from the 70, 76, or 86 nm nanodisks. Figure 4 shows the resulting (a) Gaussian versus (b) model fits for 45 independent dye molecules confined to the first quadrant of the nanodisk plane for the 76 nm nanodisk (other quadrants behave analogously by symmetry). Fits for other nanodisk diameters and dye orientations can be found in Figures S4–S9. Absent from the simulations is the substrate as well as any inherent noise associated with the experimental image acquisition. Each numerical image is generated at an artificially high resolution of 3.3 nm (panels a, b) as well as at the same effective magnification as experiment (48.5 nm pixels, panels c, d). For each molecular position (black dot) and orientation (black horizontal line), the image is fit with the four free parameters: x, y, θ, and φ. (x, y) are the predicted dye molecule centroid positions (green dots) in the plane of the nanodisk, and (θ, φ) are angles describing the predicted 3D orientation of the transition dipole moment of each molecule with θ being the polar angle and φ being the azimuthal angle in the xy-plane; the latter are represented by gray arrows indicating the angle (φ) of the molecular dipole projected into the focal plane (direction of the arrows) and the angle (θ) of the molecule from the optical axis (directly out of the page, included as the color of the arrows).

In comparing the high-resolution images in Figure 4a,b, the image model significantly outperforms Gaussian fitting, but both approaches break down for dye–nanodisk separations $\lesssim$10 nm. At the experimental image resolution of 48.5 nm (Figure 4c,d), the model can nearly exactly locate the dye in some regions while in others it is comparable to Gaussian fitting, and both approaches again perform poorly for dye–nanodisk separations $\lesssim$10 nm. This shortcoming should be expected from the underlying assumption of the model that the plasmon's optical response is restricted to dipole order. It is well established that a point source ~10 nm from a plasmonic nanoparticle will drive higher order modes,[4] and we should expect here that an accurate treatment of the quadrupole PSF will be required to infer the correct molecule location at these close separation distances.

Although the model fits to simulation suggest that the experimental molecules may lie too close to the nanodisks for the model to perform optimally, the ultimate test is to fit the model to experimental data. To assess model performance, we also simulated the expected experimental configuration and compared the predicted molecule locations in both scenarios in Figure 5. After simulation of the diffraction-limited images of 1000 dye molecules located 10.2 nm from each nanodisk edge, Figure 5a–c displays the predicted dye locations (Gaussian fits in blue and model fits in orange) summarizing the overall comparison between Gaussian and model fitting for the 70, 76, and 86 nm nanodisks. Assuming the dye molecules will have restricted rotational freedom due to their covalent bonds to each DNA linker, the simulated dye molecules' transition moments are randomly oriented in the plane perpendicular the DNA linker, and the same effective magnification was used in the simulations as the experiments. For comparison, histograms corresponding to 25 nm dye–nanodisk separation are shown in Figure S10. In the absence of

https://doi.org/10.1021/acs.jpcc.1c07989
J. Phys. Chem. C 2021, 125, 24531–24539

experimental noise, the histograms in Figure 5a–c show that the image model (orange) performs better than Gaussian fitting (blue) in locating the true molecule position (dashed vertical line) at all three nanodisk sizes, even though all higher-order plasmon modes are missing from the model. Likely due to this omission, a bimodal distribution is apparent in the model-predicted molecule location for all nanodisks with one mode coinciding favorably with the true molecular position.

Despite its restriction to the dipole plasmon response, we can also apply the image model to the experimental data where the dye molecules are known to be 10.2 nm from the nanodisk edge due to the fixed length of their DNA linkers. As described above, the image model fitting procedure follows that for the simulated images. Specifically, it starts by parametrizing the coupled dipole model on the individual, single-particle scattering spectra of the three nanodisks. This step of the parametrization yields the oscillator properties of the gold nanodisk. The oscillator properties of the dye molecule's emissive transition are taken to be that of a simple harmonic oscillator fit to the dye emission spectrum. The last step is to estimate the nanodisk location, which is done by fitting a simple 2D Gaussian to the background image that is dominated by the plasmon photoluminescence.[14] The parametrized model is then fit to each experimental image with the six free parameters: x, y,θ, φ, A, and c. Here, (A, c) are the additional multiplicative amplitude and offset needed because the model does not account for the brightness of the image generated by absorption enhancement effects (Figure S3).

Figure 5d–f displays the fit locations (Gaussian fits in blue and model fits in orange) based on a representative subset of the background-subtracted experimental images (1000–2000 single-molecule images per nanodisk size). Gaussian fitting returns dye locations that are largely mislocalized inward toward the nanodisk, while the image model results again in a bimodal distribution straddling the true molecule location. Furthermore, separately considering the data for molecule fits with polar angle, θ, nearly aligned with the focal axis vs θ nearly perpendicular to the focal axis, reveals that in these experiments the fit positions of molecules predicted to be oriented near the focal plane are systematically closer to the true molecule location (Figures S11 and S12).

The molecular orientation dependence of each of these modes shows that molecules predicted to reside too close to the nanodisk (i.e., the inner misfit population) are predominantly oriented with transition dipoles along the focal axis and the outer misfit molecules are predominantly oriented with transition dipoles perpendicular to its DNA linker in the plane of the nanodisk (Figures S13 and S14). This result is consistent with our assumption that the molecules are constrained to rotate in a plane perpendicular to their DNA linkers, and it suggests that the dipole-restricted model may be better at predicting the true molecule orientations than their locations. In part, the analogous fits to simulated images further support this hypothesis since molecules were simulated to orient within this plane and fit results demonstrate similar trends (Figures S13 and S14).

Because this result is only partially consistent with model fits to simulation (Figures S13 and S14), the bifurcation of fit-predicted molecule locations could result from compensating for physics absent from the model. For example, if they are active, plasmonic quadrupoles will generate their own image fields that will interfere with both molecular and image dipole fields. These effects on the image may be interpreted by the dipole–dipole model as a molecule that resides at a slightly different position. Another explanation for the differences is that although the model accounts for the substrate in the parametrization process, an isotropic background is otherwise assumed. If the anisotropy of the background medium affects dipole–dipole coupling in opposite ways for different dipole orientations, then the observed fit bifurcations may be explained. Finally, our fits to simulation in Figure 4 demonstrate drastic improvement in model performance when the image magnification is enhanced (without loss of signal). Although the experimental magnification is limited by the experimental signal-to-noise ratio, it is possible that further information could be extracted from experiment to yield a similar improvement. One possibility would be to simultaneously measure single-molecule images and spectra. With a model that predicts both observables, higher precision in molecule-location estimation will likely result.

CONCLUSION

We have engineered single-particle assemblies consisting of a gold nanodisk surrounded by ATTO590 dye molecules attached by double-stranded DNA linkers. These assemblies make up a controlled geometry that places plasmon-coupled dye molecules at specific radial positions in the plane of the nanodisk and provide the ground truth actual dye molecule position for further analysis. We used the known components of the system to derive a coupled-dipole model of the emission, and we fit simulated and experimental data with the model function as well as to a standard Gaussian function. We find that the image model cannot perfectly recapture the true dye molecule position, and we attribute the disagreement between the image model and experiment to the insufficient data resolution and to missing physics in the modeling of the nanodisk–plasmon response. Nevertheless, there is a clear path for improvement of the image model and of our experiment. Future work will focus on integrating higher-order plasmon multipole effects into the nanodisk response as well as simultaneously using coupled dye–nanodisk emission spectra alongside the microscope images in our fits. Working with longer DNA spacers that position the dye molecules further away from the regime where more complex dye–nanodisk interactions occur will also play a critical role in benchmarking the model.

ASSOCIATED CONTENT

Supporting Information

The Supporting Information is available free of charge at https://pubs.acs.org/doi/10.1021/acs.jpcc.1c07989.

Experimental and calculated dark-field spectra; ellipsometry characterization; plasmon-coupled fluorescence enhancement; fit positions and angles for all considered geometries; histograms of radial fit locations and model-predicted dye orientations; sequences of oligonucleotides used in this study (PDF)

AUTHOR INFORMATION

Corresponding Authors

Julie S. Biteen − *Department of Chemistry, University of Michigan, Ann Arbor, Michigan 48109, United States;* orcid.org/0000-0003-2038-6484; Email: jsbiteen@umich.edu

David J. Masiello − *Department of Chemistry, University of Washington, Seattle, Washington 98195, United States;* orcid.org/0000-0002-1187-0920; Email: masiello@uw.edu

Authors

Tiancheng Zuo − *Department of Chemistry, University of Michigan, Ann Arbor, Michigan 48109, United States;* orcid.org/0000-0003-1278-1820

Harrison J. Goldwyn − *Department of Chemistry, University of Washington, Seattle, Washington 98195, United States;* orcid.org/0000-0002-7184-2120

Complete contact information is available at: https://pubs.acs.org/10.1021/acs.jpcc.1c07989

Author Contributions

T.Z. and H.J.G. contributed equally to this work.

Notes

The authors declare no competing financial interest.

■ ACKNOWLEDGMENTS

Work at the University of Michigan was supported by National Science Foundation (NSF) Grant CHE-1807676 to J.S.B., and work at the University of Washington was supported NSF grants CHE-1954393 and CHE-2118333 to D.J.M.

■ REFERENCES

(1) Yuan, H.; Khatua, S.; Zijlstra, P.; Yorulmaz, M.; Orrit, M. Thousand-Fold Enhancement of Single-Molecule Fluorescence Near a Single Gold Nanorod. *Angew. Chem., Int. Ed.* **2013**, *52* (4), 1217−1221.

(2) Akselrod, G. M.; Argyropoulos, C.; Hoang, T. B.; Ciracì, C.; Fang, C.; Huang, J.; Smith, D. R.; Mikkelsen, M. H. Probing the Mechanisms of Large Purcell Enhancement in Plasmonic Nanoantennas. *Nat. Photonics* **2014**, *8* (11), 835−840.

(3) Kinkhabwala, A.; Yu, Z.; Fan, S.; Avlasevich, Y.; Mullen, K.; Moerner, W. E. Large Single-Molecule Fluorescence Enhancements Produced by a Gold Bowtie Nanoantenna. *Nat. Photonics* **2009**, *3*, 654−657.

(4) Novotny, L.; Hecht, B. *Principles of Nano-Optics*, 2nd ed.; Cambridge University Press: Cambridge, UK, 2012.

(5) Lee, S. A.; Biteen, J. S. Interplay of Nanoparticle Resonance Frequency and Array Surface Coverage in Live-Cell Plasmon-Enhanced Single-Molecule Imaging. *J. Phys. Chem. C* **2018**, *122* (10), 5705−5709.

(6) Boutelle, R. C.; Neuhauser, D.; Weiss, S. Far-Field Super-Resolution Detection of Plasmonic Near-Fields. *ACS Nano* **2016**, *10* (8), 7955−7962.

(7) Ropp, C.; Cummins, Z.; Nah, S.; Fourkas, J. T.; Shapiro, B.; Waks, E. Nanoscale Probing of Image-Dipole Interactions in a Metallic Nanostructure. *Nat. Commun.* **2015**, *6*, 6558.

(8) Steuwe, C.; Erdelyi, M.; Szekeres, G.; Csete, M.; Baumberg, J. J.; Mahajan, S.; Kaminski, C. F. Visualizing Electromagnetic Fields at the Nanoscale by Single Molecule Localization. *Nano Lett.* **2015**, *15* (5), 3217−3223.

(9) Zuo, T.; Goldwyn, H. J.; Isaacoff, B. P.; Masiello, D. J.; Biteen, J. S. Rotation of Single-Molecule Emission Polarization by Plasmonic Nanorods. *J. Phys. Chem. Lett.* **2019**, *10* (17), 5047−5054.

(10) Lee, S. A.; Biteen, J. S. Spectral Reshaping of Single Dye Molecules Coupled to Single Plasmonic Nanoparticles. *J. Phys. Chem. Lett.* **2019**, *10* (19), 5764−5769.

(11) Moerner, W. E. Examining Nanoenvironments in Solids on the Scale of a Single, Isolated Molecule. *Science* **1994**, *265*, 46−53.

(12) Chattopadhyay, S.; Biteen, J. S. Super-Resolution Characterization of Heterogeneous Light−Matter Interactions between Single Dye Molecules and Plasmonic Nanoparticles. *Anal. Chem.* **2021**, *93* (1), 430−444.

(13) Thompson, R. E.; Larson, D. R.; Webb, W. W. Precise Nanometer Localization Analysis for Individual Fluorescent Probes. *Biophys. J.* **2002**, *82*, 2775−2783.

(14) Isaacoff, B. P.; Li, Y.; Lee, S. A.; Biteen, J. S. SMALL-LABS: Measuring Single-Molecule Intensity and Position in Obscuring Backgrounds. *Biophys. J.* **2019**, *116* (6), 975−982.

(15) Maus, M.; Cotlet, M.; Hofkens, J.; Gensch, T.; De Schryver, F. C.; Schaffer, J.; Seidel, C. A. M. An Experimental Comparison of the Maximum Likelihood Estimation and Nonlinear Least-Squares Fluorescence Lifetime Analysis of Single Molecules. *Anal. Chem.* **2001**, *73* (9), 2078−2086.

(16) Wertz, E. A.; Isaacoff, B. P.; Biteen, J. S. Wavelength-Dependent Super-Resolution Images of Dye Molecules Coupled to Plasmonic Nanotriangles. *ACS Photonics* **2016**, *3* (10), 1733−1740.

(17) Goldwyn, H. J.; Smith, K. C.; Busche, J. A.; Masiello, D. J. Mislocalization in Plasmon-Enhanced Single-Molecule Fluorescence Microscopy as a Dynamical Young's Interferometer. *ACS Photonics* **2018**, *5* (8), 3141−3151.

(18) Mack, D.; Cortés, E.; Giannini, V.; Török, P.; Roschuk, T.; Maier, S. Decoupling Absorption and Emission Processes in Super-Resolution Localization of Emitters in a Plasmonic Hotspot. *Nat. Commun.* **2017**, *8*, 14513.

(19) Heaps, C. W.; Schatz, G. C. Modeling Super-Resolution SERS Using a T-Matrix Method to Elucidate Molecule-Nanoparticle Coupling and the Origins of Localization Errors. *J. Chem. Phys.* **2017**, *146* (22), 224201.

(20) Lim, K.; Ropp, C.; Barik, S.; Fourkas, J.; Shapiro, B.; Waks, E. Nanostructure-Induced Distortion in Single-Emitter Microscopy. *Nano Lett.* **2016**, *16* (9), 5415−5419.

(21) Raab, M.; Vietz, C.; Stefani, F. D.; Acuna, G. P.; Tinnefeld, P. Shifting Molecular Localization by Plasmonic Coupling in a Single-Molecule Mirage. *Nat. Commun.* **2017**, *8*, 13966.

(22) Blythe, K. L.; Willets, K. A. Super-Resolution Imaging of Fluorophore-Labeled DNA Bound to Gold Nanoparticles: A Single-Molecule, Single-Particle Approach. *J. Phys. Chem. C* **2016**, *120* (2), 803−815.

(23) Baiyasi, R.; Jebeli, S. A. H.; Zhang, Q.; Su, L.; Hofkens, J.; Uji-i, H.; Link, S.; Landes, C. F. PSF Distortion in Dye−Plasmonic Nanomaterial Interactions: Friend or Foe? *ACS Photonics* **2019**, *6* (3), 699−708.

(24) Blanquer, G.; van Dam, B.; Gulinatti, A.; Acconcia, G.; De Wilde, Y.; Izeddin, I.; Krachmalnicoff, V. Relocating Single Molecules in Super-Resolved Fluorescence Lifetime Images near a Plasmonic Nanostructure. *ACS Photonics* **2020**, *7* (2), 393−400.

(25) Wertz, E.; Isaacoff, B. P.; Flynn, J. D.; Biteen, J. S. Single-Molecule Super-Resolution Microscopy Reveals How Light Couples to a Plasmonic Nanoantenna on the Nanometer Scale. *Nano Lett.* **2015**, *15* (4), 2662−2670.

(26) Taylor, A. B.; Zijlstra, P. Single-Molecule Plasmon Sensing: Current Status and Future Prospects. *ACS Sens.* **2017**, *2* (8), 1103−1122.

(27) Blythe, K. L.; Titus, E. J.; Willets, K. A. Comparing the Accuracy of Reconstructed Image Size in Super-Resolution Imaging of Fluorophore-Labeled Gold Nanorods Using Different Fit Models. *J. Phys. Chem. C* **2015**, *119* (33), 19333−19343.

(28) Ayala-Orozco, C.; Liu, J. G.; Knight, M. W.; Wang, Y.; Day, J. K.; Nordlander, P.; Halas, N. J. Fluorescence Enhancement of Molecules Inside a Gold Nanomatryoshka. *Nano Lett.* **2014**, *14*, 2926−2933.

(29) Anger, P.; Bharadwaj, P.; Novotny, L. Enhancement and Quenching of Single-Molecule Fluorescence. *Phys. Rev. Lett.* **2006**, *96*, 113002.

(30) Fu, B.; Flynn, J. D.; Isaacoff, B. P.; Rowland, D. J.; Biteen, J. S. Super-Resolving the Distance-Dependent Plasmon-Enhanced Fluorescence of Single Dye and Fluorescent Protein Molecules. *J. Phys. Chem. C* **2015**, *119* (33), 19350−19358.

(31) Kongsuwan, N.; Demetriadou, A.; Chikkaraddy, R.; Benz, F.; Turek, V. A.; Keyser, U. F.; Baumberg, J. J.; Hess, O. Suppressed Quenching and Strong-Coupling of Purcell-Enhanced Single-Molecule Emission in Plasmonic Nanocavities. *ACS Photonics* **2018**, *5* (1), 186−191.
(32) Taylor, A.; Verhoef, R.; Beuwer, M.; Wang, Y.; Zijlstra, P. All-Optical Imaging of Gold Nanoparticle Geometry Using Super-Resolution Microscopy. *J. Phys. Chem. C* **2018**, *122* (4), 2336−2342.
(33) Chikkaraddy, R.; Turek, V. A.; Kongsuwan, N.; Benz, F.; Carnegie, C.; van de Goor, T.; de Nijs, B.; Demetriadou, A.; Hess, O.; Keyser, U. F.; et al. Mapping Nanoscale Hotspots with Single-Molecule Emitters Assembled into Plasmonic Nanocavities Using DNA Origami. *Nano Lett.* **2018**, *18* (1), 405−411.
(34) Chikkaraddy, R.; de Nijs, B.; Benz, F.; Barrow, S. J.; Scherman, O. A.; Rosta, E.; Demetriadou, A.; Fox, P.; Hess, O.; Baumberg, J. J. Single-Molecule Strong Coupling at Room Temperature in Plasmonic Nanocavities. *Nature* **2016**, *535* (7610), 127−130.
(35) Fu, B.; Isaacoff, B. P.; Biteen, J. S. Super-Resolving the Actual Position of Single Fluorescent Molecules Coupled to a Plasmonic Nanoantenna. *ACS Nano* **2017**, *11* (9), 8978−8987.
(36) Johnson, P. B.; Christy, R. W. Optical Constants of Noble Metals. *Phys. Rev. B* **1972**, *6*, 4370−4379.
(37) Hurst, S. J.; Lytton-Jean, A. K. R.; Mirkin, C. A. Maximizing DNA Loading on a Range of Gold Nanoparticle Sizes. *Anal. Chem.* **2006**, *78* (24), 8313−8318.
(38) Oh, J.-H.; Park, D. H.; Joo, J. H.; Lee, J.-S. Recent Advances in Chemical Functionalization of Nanoparticles with Biomolecules for Analytical Applications. *Anal. Bioanal. Chem.* **2015**, *407* (29), 8627−8645.
(39) Heilemann, M.; van de Linde, S.; Schüttpelz, M.; Kasper, R.; Seefeldt, B.; Mukherjee, A.; Tinnefeld, P.; Sauer, M. Subdiffraction-Resolution Fluorescence Imaging with Conventional Fluorescent Probes. *Angew. Chem., Int. Ed.* **2008**, *47* (33), 6172−6176.
(40) van de Linde, S.; Löschberger, A.; Klein, T.; Heidbreder, M.; Wolter, S.; Heilemann, M.; Sauer, M. Direct Stochastic Optical Reconstruction Microscopy with Standard Fluorescent Probes. *Nat. Protoc.* **2011**, *6* (7), 991−1009.
(41) Hohenester, U.; Trügler, A. MNPBEM − A Matlab Toolbox for the Simulation of Plasmonic Nanoparticles. *Comput. Phys. Commun.* **2012**, *183* (2), 370−381.
(42) Record, M. T.; Mazur, S. J.; Melancon, P.; Roe, J. H.; Shaner, S. L.; Unger, L. Double Helical DNA: Conformations, Physical Properties, and Interactions with Ligands. *Annu. Rev. Biochem.* **1981**, *50* (1), 997−1024.
(43) Bohren, C. F.; Huffman, D. R. *Absorption and Scattering of Light by Small Particles*; Wiley: New York, 1983.

https://doi.org/10.1021/acs.jpcc.1c07989
J. Phys. Chem. C 2021, 125, 24531−24539